

# Damage Detection Using High-Resolution SAR Imagery in the 2009 L'Aquila, Italy, Earthquake

Pralhad Uprety,<sup>a)</sup> Fumio Yamazaki,<sup>a)</sup> MEERI, and Fabio Dell'Acqua<sup>b)</sup>

Satellite remote sensing is being used to monitor disaster-affected areas for post-disaster reconnaissance and recovery. One of the special features of Synthetic Aperture Radar (SAR) is that it can operate day and night and penetrate the cloud cover because of which it is being widely used in emergency situations. Building damage detection for the 6 April 2009 L'Aquila, Italy, earthquake was conducted using high-resolution TerraSAR-X images obtained before and after the event. The correlation coefficient and the difference of backscatter coefficients of the pre- and post-event images were calculated in a similar way as [Matsuoka and Yamazaki \(2004\)](#). The threshold value of the correlation coefficient was suggested and used in detecting building damage. The results were compared with ground truth data and a post-event optical image. Based on the study, building damage could be observed in an urban setting of L'Aquila with overall accuracy of 89.8% and Kappa coefficient of 0.45. [DOI: 10.1193/060211EQS126M]

## INTRODUCTION

Disasters have been defined as events that cause serious disruption in a community or a society, resulting in widespread human, material, economic and environmental losses ([ISDR 2010](#)). Recent examples of disasters that caused very precarious situation in different parts of the world include the 2011 Tohoku, Japan, earthquake, the 2010 Haiti earthquake, and the 2010 Pakistan flood, all of which caused immense loss of lives and properties. Timely action and response with regard to a disaster situation is extremely important. Remote sensing, in particular satellite remote sensing, is of great help because it can provide the data of a largely affected region without being there physically. Remote sensing technology has been successfully utilized for assessing the damage distribution from disasters ([Huyck et al. 2002](#), [Saito and Spence 2004](#), [Yamazaki et al. 2005](#)). Remote sensing technology is useful in all phases of emergency management cycle (mitigation, preparedness, response, and recovery).

Generally, the satellite system employs either optical or microwave sensors. Commercial satellites, such as Ikonos, QuickBird, GeoEye, and WorldView, use optical sensors while Radarsat and ALOS/PALSAR use microwave sensors. Optical sensors can be used only during daytime without cloud cover, whereas synthetic aperture radar (SAR) is free from these constraints. SAR is a powerful tool and has been utilized in various disaster situations

---

<sup>a)</sup> Department of Urban Environment System, Graduate School of Engineering, Chiba University, 1-33 Yayoi-cho, Inage-ku, Chiba 263-8522, Japan

<sup>b)</sup> Department of Electronics, University of Pavia, 1-27100 Pavia, Italy

including earthquakes because of these characteristics (Matsuoka and Yamazaki 2004, 2010, Stramondo et al. 2006, Rathje and Adams 2008, Dell'Acqua et al. 2010, Thao et al. 2010).

SAR is an active sensor illuminating a target with its own energy and then recording a portion of the energy reflected back to it (also called backscatter). It can be operated day and night and is independent of climatic condition, which makes it more efficient for the disaster situations. SAR creates a comparatively high pixel-resolution as it simulates a long antenna by combining electrical signals received by its sensor as it moves along a particular track. Each pixel in intensity (amplitude) image corresponds to radar backscattering from the target. The backscattering coefficient is dependent on the local incidence angle of microwave, electrical characteristics, surface roughness, moisture content of the target and the wavelength of microwave. Open surface or damaged buildings show low backscatter because of scattered reflection. The corner reflection of buildings depends on the height and the aspect angle (Balz et al. 2010). The aspect angle refers to the orientation of a building relative to the viewing direction of radar. The backscattering coefficients obtained from pre- and post-event SAR images can be used for change/damage detection (Yonezawa and Takeuchi 2001, Matsuoka and Yamazaki 2004, Stramondo et al. 2006, Gamba and Dell'Acqua 2007).

Recently, the resolution of satellite SAR systems has been improved significantly with the launch of TerraSAR-X and COSMO/SkyMed. Regarding the 2009 L'Aquila, Italy, earthquake, Dell'Acqua et al. (2010) have used only a post-event SAR image from COSMO/SkyMed to estimate damage level aggregated at the size of city block level. However, the present paper may be the first trial to investigate individual buildings' damage using pre- and post-event high-resolution TerraSAR-X imagery for the 2009 L'Aquila, Italy, earthquake. Using the pre- and post-event high-resolution SAR intensity images, the change detection is carried out using the method similar to Matsuoka and Yamazaki (2004) for the building damage detection at an individual level after the earthquake and the result is compared with ground truth data and pre- and post-event QuickBird images.

## THE L'AQUILA EARTHQUAKE AND DATA EMPLOYED

L'Aquila is a historical town in the central Abruzzo region of Italy (Figure 1) and is located 110 km northeast of Rome. It is also the largest city in the region. Most of the buildings are masonry (68%), followed by reinforced concrete (24%), and others (8%) (ISTAT 2001, cited by Cosenza et al. 2009).

Italy in general and the L'Aquila area in particular have been severely affected by numerous earthquakes in the past. Notable past earthquakes occurred in 1315, 1349, 1461, 1703, 1706, 1915, and 1958 (Stucchi et al. 2010). An earthquake of moment-magnitude ( $M_w$ ) 6.3 hit the central Abruzzo region of Italy on 6 April 2009 at 3:32 a.m. local time, affecting many human settlements throughout the region. The epicentre was located at 42.334°N, 13.334°E with the depth 8.8 km (USGS 2010). This earthquake severely affected the old city of L'Aquila. Three hundred seven (307) people were killed (Fidani 2010), more than 1,500 people sustained injuries (Celebi et al. 2010), and about 65,000 people were rendered homeless by this earthquake. This event is the deadliest one to hit Italy since the 1980 Irpinia earthquake. Many important structures, including San Salvatore Hospital, had to be evacuated due to the high damage level (Casarotti et al. 2010). Many historical buildings,

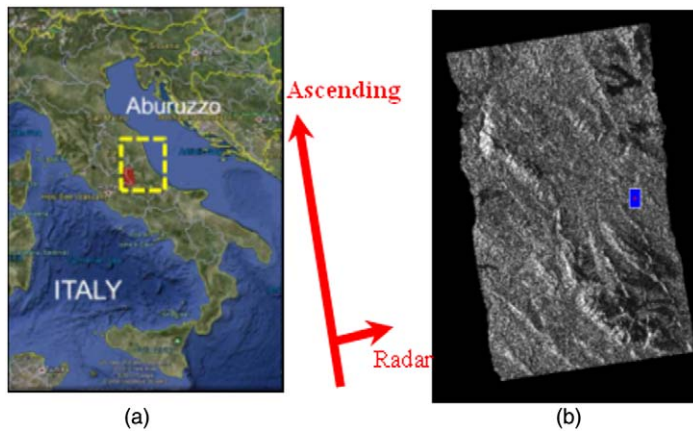


**Figure 1.** Location of the study area; (a) location of Aburuzzo region (yellow dotted line), Italy. L'Aquila city lies in the Aburuzzo region. Red rectangle shows the geographic area (area 1,982 km<sup>2</sup>) covered by TerraSAR-X images on the map of Italy in Google Earth, and (b) the post-event SAR image (Apr. 13, 2009) of the area. Blue rectangle shows the study area (area 6.7 km<sup>2</sup>) which includes the old city of L'Aquila. The path of TerraSAR-X was ascending with a right-looking mode.

including L'Aquila castle and Collemaggio Church, were heavily damaged (Celebi et al. 2010).

Data employed in this research are intensity images from the TerraSAR-X satellite system. TerraSAR-X is a satellite with a right-side-looking active phased array antenna technology (DLR 2009). It works at X-band, specifically at a wavelength of 3.11 cm (frequency of 9.65 GHz). The SAR intensity images used in this research were a pre-event one, acquired about two months before (6 February 2009), and a post-event one, which was obtained seven days after (13 April 2009) the earthquake. The acquisition mode was StripMap with HH polarization and incidence angle 39.2 degrees from the ascending path. These images have a spatial resolution of about 3 m with a pixel spacing of 1.25 m. The employed data was Enhanced Ellipsoid Corrected (EEC) product with map geometry, projected into the WGS84 reference ellipsoid. The resolution mode was SE (spatially enhanced) high resolution (DLR 2009), and hence the multi-look images have azimuth looks of 1.02 and range looks of 1.07, as written in the data header file.

Pan-sharpened QuickBird images with 0.6 m resolution were also employed to assess the results from the TerraSAR-X data. The pre-event image was obtained about 19 months before (4 September 2006) and the post-event one was obtained after two days (8 April 2009) following the earthquake.

## DAMAGE DETECTION METHODOLOGY

First, the study area, with an area of 6.7 km<sup>2</sup> was chosen in the city center of the L'Aquila. Then we selected the area within the SAR (Figure 2) and optical images. After this, nearest

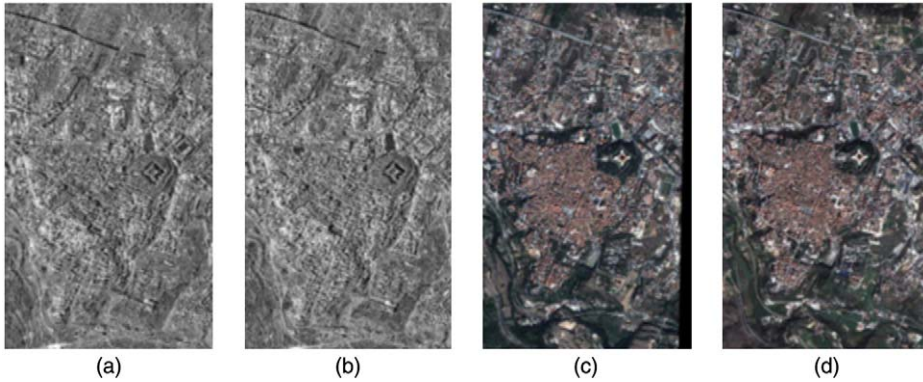


**Figure 2.** Calibrated TerraSAR-X intensity images and optical images in study area in L'Aquila city (a) pre-event SAR image (6 February 2009), (b) post-event SAR image (13 April 2009), (c) pre-event QuickBird image (4 September 2006), and (d) post-event QuickBird image (8 April 2009).

neighborhood re-sampling of the SAR images were carried out, changing the pixel size from 1.25 m to 0.6 m so that they can be compared with the pan-sharpened 0.6 m QuickBird images. The pan-sharpening of the optical images was conducted using the principal component (PC) sharpening method. Regarding the speckle removal in the SAR data, Lee adaptive filter (Lee 1980) was used. The adaptive filter produces an accurate estimate of the backscattering coefficient inside homogeneous stationary areas while preserving edge and texture therefore preferred for SAR imagery. We want to retain the texture as much as possible, with less noise as far as possible. For this, we selected the filter size of  $11 \times 11$  (6.6 m  $\times$  6.6 m) out of different candidates:  $9 \times 9$ ,  $11 \times 11$ ,  $13 \times 13$ , and  $15 \times 15$ , to remove speckle noise from each image. Then each intensity image was converted to the backscattering coefficient in the ground range ( $\sigma_0$ ) using Equations 1, 2, and 3 (Infoterra 2008, Breit et al. 2010).

$$\sigma_0 (db) = \beta_0 (db) + 10 \log_{10}(\sin(\theta_{loc})), \quad (1)$$

where

$$\beta_0 = 10 \log_{10}(\text{Calibration factor} * DN^2) \quad (2)$$

$$\theta_{loc} = [GIM - (GIM \bmod 10)] / 100 \quad (3)$$

Here  $\beta_0$  refers to the backscatter per unit area in the slant range and  $\sigma_0$  refers to backscatter per unit area in the ground range. Geo-coded incidence angle mask (GIM) gives the local incidence angle, which represents the angle between the radar beam and the normal to the illuminated surface.  $GIM \bmod 10$  represents the remainder of the division of GIM by 10. The resulting incidence angle is in degree (float value).

Following this, the pre-event SAR image was taken as the master and the post-event SAR image and pan-sharpened pre-and post-event optical images were taken as slaves, and the

subsequent co-registration was carried out at a sub-pixel level. Finally, two parameters, namely the backscattering difference value ( $d$ ) and the correlation coefficient ( $r$ ), were calculated within a different pixel window sizes:  $7 \times 7$ ,  $9 \times 9$ , and  $11 \times 11$ , for the pre- and post-event images using Equations 4 and 5. We found that there was no significant difference and hence we adopted  $9 \times 9$  pixel window ( $5.4 \text{ m} \times 5.4 \text{ m}$ ) considering the building size as well as to accommodate small changes after the earthquake.

$$d = \bar{I}a_i - \bar{I}b \quad (4)$$

$$r = \frac{N \sum_{i=1}^N I a_i I b_i - \sum_{i=1}^N I a_i \sum_{i=1}^N I b_i}{\sqrt{\left( N \sum_{i=1}^N I a_i^2 - \left( \sum_{i=1}^N I a_i \right)^2 \right) \cdot \left( N \sum_{i=1}^N I b_i^2 - \left( \sum_{i=1}^N I b_i \right)^2 \right)}} \quad (5)$$

where  $I a_i$ ,  $I b_i$  represent the  $i$ -th pixel values (backscattering coefficients) of the post- and pre-event images, respectively and  $\bar{I}a_i$ ,  $\bar{I}b_i$  are the average values of the  $9 \times 9$  pixels surrounding the  $i$ -th pixel. The correlation coefficient ( $r$ ) is a scalar quantity and its value ranges between  $-1$  to  $1$ . High positive value of  $r$  indicates no change between the pre- and post-event images while a low value of  $r$  indicates strong possibility of change between the two images (Brown 1992). Similarly, the normalized difference vegetation index (NDVI) was calculated using Equation 6 from the pre-event pan-sharpened QuickBird image to observe non-vegetated parts in the study area.

$$NDVI = (NIR - R)/(NIR + R) \quad (6)$$

where  $NIR$  and  $R$  represent the digital numbers of a pixel in the near-infrared band and the red band, respectively. The  $NDVI$  value ranges from  $-1$  to  $+1$  and represents the activity of chlorophyll containing biomass. The  $NDVI$  was evaluated to see the built-up and vegetated areas within the study area.

The center of the city core is a high-density area. The radar backscatters from buildings are very complex and hence, we could not detect building damage at an individual level using the SAR images. Therefore, we opted for a moderately dense area for testing our damage detection technique. For this purpose, 118 buildings were digitized in a GIS environment using the vertical pre-event QuickBird image. The heavily damaged buildings (Grade 5 in the EMS scale) were identified by comparing the pre- and post-event QuickBird images. Cross check was conducted using the damaged building footprints provided by the Italian Civil Protection Agency, originally generated from post-event, 15 cm ground resolution aerial images (acquired by the Italian Air Force and visually interpreted by their professionals) as well as from other sources including Tertulliani et al. (2010).

There were 118 buildings under investigation, out of which eight were of damage Grade 5, 12 of damage Grade 4 and rest were damage Grades 1–3 per the EMS scale. Though the G5 buildings were few, these are all the damaged (G5) buildings in this area. In order to find damaged buildings using the backscatter characteristics,  $r$  and  $d$ , the average values of these indices were calculated within each building footprint. When we plotted the graph of  $r$  and  $d$

for Grade 5, Grade 4, and Grades 1–3, it was found that values of damage Grade 4 and Grades 1–3 were similar so we combined these two groups into damage Grades 1–4. However, when we plotted a graph between the difference and correlation coefficient with mean and standard deviation of Grade 5 and Grades 1–4 buildings, we found that the variation of the difference is too large, indicating that a linear discriminate analysis with these two parameters has low sensitivity. Another reason might be the smaller number of collapsed buildings (less than 10%) compared with the less damaged buildings (Grades 1–4). It is to be noted that less damaged category namely G1 also includes no damage class. Therefore correlation coefficient was only used to characterize damage status. Although the difference of the back-scattering coefficients was not so effective for damage detection in our example, the parameter was found to be useful in other examples, especially for detecting buildings with severely damaged walls (Liu et al. 2012).

The threshold value for low correlation was selected by trial and error to judge the buildings under investigation into two classes: Grade 5 and Grades 1–4. Finally an error matrix was prepared to see the accuracy of our damage detection using the SAR data in individual building level. ‘Kappa or KHAT’ coefficient was also evaluated, which is used as an indicator to find out the extent to percentage correct values of an error matrix, are due to “true” agreement versus chance (Lillesand et al. 2004). The Kappa value ranges from  $-1.0$  to  $1.0$ , with  $-1.0$  indicating perfect disagreement below chance,  $0.0$  indicating agreement equal to chance, and  $1.0$  indicating perfect agreement above chance. Kappa values are also divided into three classes: a value greater than  $0.80$  (80%) represents strong agreement, whereas the value between  $0.40$  and  $0.80$  (40% to 80%) represents moderate agreement, and a value below  $0.40$  (40%) represents poor agreement (Congalton 1996). Figure 3 shows the flowchart of methodology adopted in this study.

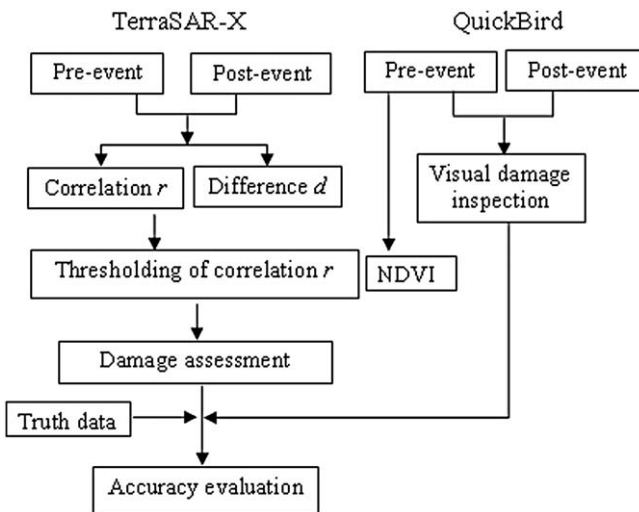
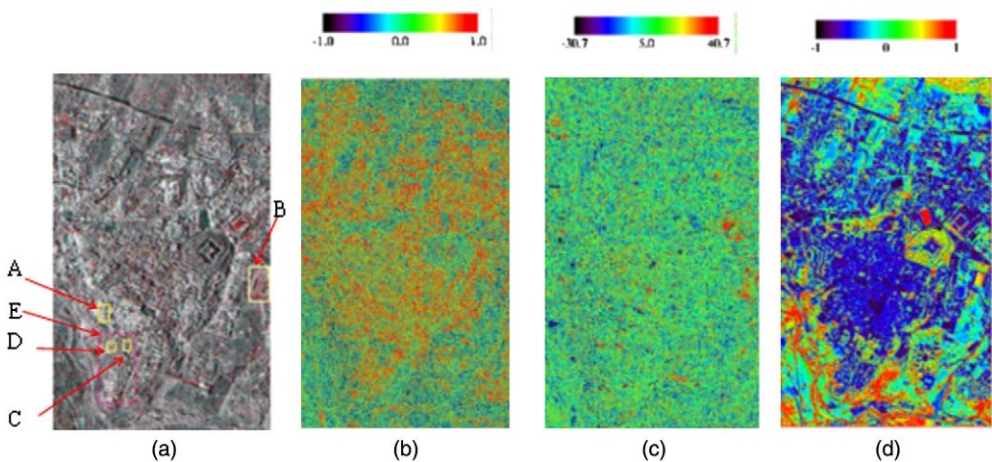


**Figure 3.** Flow chart of methodology adopted in this study.

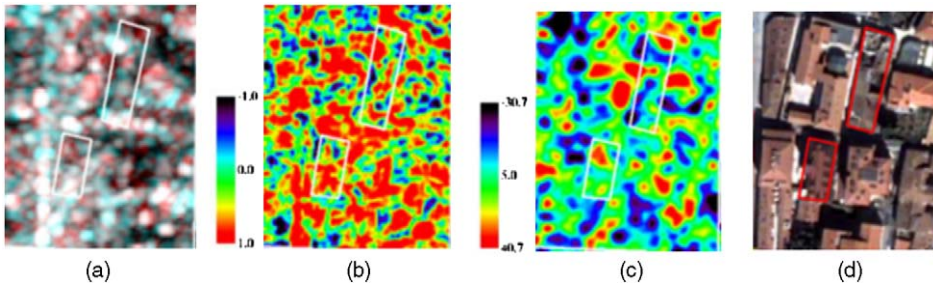
## RESULTS AND DISCUSSION

Figure 4a is the color composite of the two SAR images (Red: post-event; Green, Blue: pre-event). The RGB color composite was used for a reference purpose to observe the possible areas of change. Red in the composite image indicates an increased backscatter due to the possible change by the earthquake: cyan (Blue + Green) areas represent a decreased backscatter while grey areas are the unchanged areas over the time. Figure 4b shows the correlation coefficient between the pre- and post-event images, ranging from  $-0.98$  to  $1.0$ . Figure 4c shows the difference of the backscattering coefficients, ranging from  $-30.72$  dB to  $40.70$  dB. Figure 4d is a rainbow color plot of the normalized difference vegetation index (NDVI) from the pre-event QuickBird image. High NDVI, as in vegetation, is seen with warm colors, while low NDVI, as in built-up areas, is seen in cool colors. Figure 5 shows a typical high-density area in the city core. Damaged buildings are shown with bounded polygons. The correlation is high even in the damaged buildings. Due to the side-looking nature of SAR, the backscatter characteristics are quite complex in such a dense area. This can be understood from Figure 6. Case (a) illustrates a typical example of high-density areas in the city core showing the different level of backscatter from buildings. The strength of backscatter from damage buildings changes depending upon the position to the direction of radar illumination.

Low correlation coefficients and large backscattering differences are considered to be the changes that occurred in this period, possibly caused by the earthquake. To check this, a close-up of a typical area is presented. There were many temporary settlements in an open space after the earthquake, and they were easily distinguished. An example is shown in Figure 7; the color composite shows a prominent blue color with low correlation and a red color with high backscattering difference. The post-event optical image is shown to verify this observation. Undamaged buildings show high correlation values as seen in Figure 7b. These recognitions typically represent the capacity of SAR in change detection.



**Figure 4.** (a) RGB color composite of the calibrated SAR images (R: the post-event, G, B: the pre-event) of the central L'Aquila city, (b) the correlation coefficient, (c) the backscattering difference, and (d) the NDVI from the pre-event QuickBird image.



**Figure 5.** Close-up of area A in Figure 4, showing an example of high density area. (a) RGB color composite of calibrated SAR images (R: the post event, G, B: the pre-event), (b) the correlation coefficient, (c) the backscattering difference, and (d) the post-event QuickBird image (2009.4.8). G-5 damaged buildings are shown in red polygons.

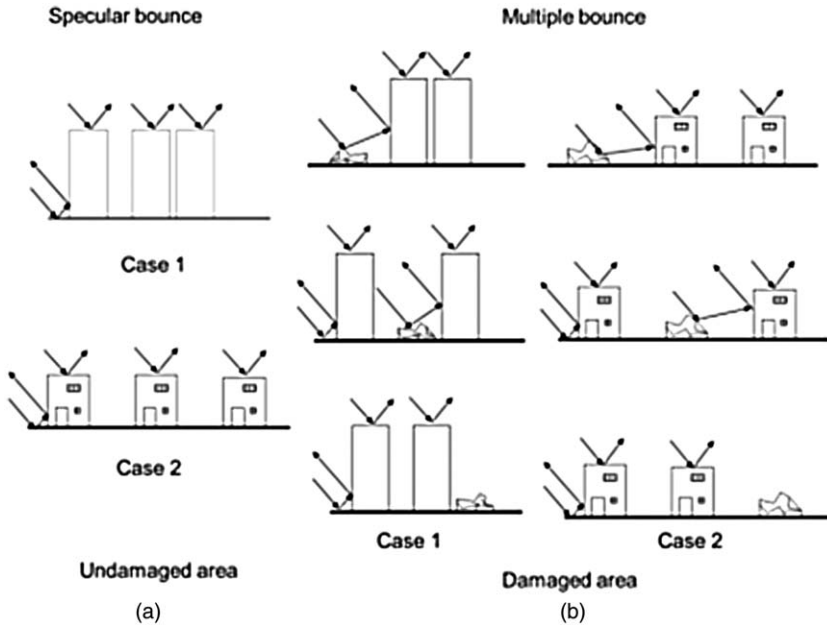


**Figure 6.** Schematic diagram of backscatter from standing buildings and when they are collapsed. (a) undamaged buildings with high density (Case 1) and with moderate density (Case 2). (b) Damaged buildings with different situations for Cases 1 and 2. A damaged building in top right shows the strongest backscatter, middle one shows weaker backscatter and bottom one shows the weakest backscatter due to radar shadow.

The color composite in Figure 8a indicates that red spots correspond to the increase of backscatter in this time interval while cyan (Blue + Green) spots correspond to the decrease of backscatter. Low correlation in Figure 8b and large backscattering difference in Figure 8c can be noticed in the areas marked with rectangles, where left and right ones have large

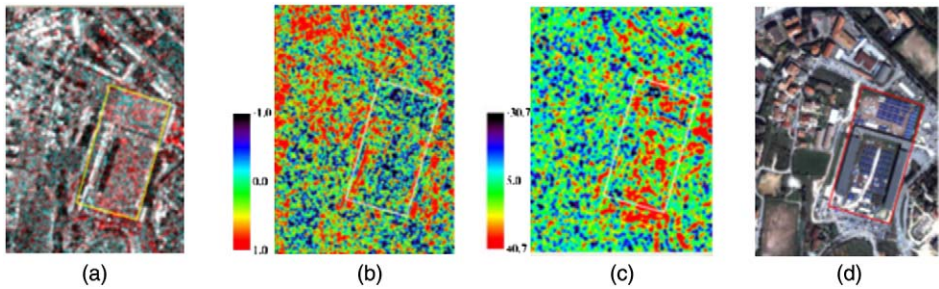


**Figure 7.** Close-up of area B in Figure 4. (a) RGB color composite of calibrated SAR images (R: the post-event, G, B: the pre-event), (b) the correlation coefficient, (c) the backscattering difference, and (d) the post-event QuickBird image (2009.4.8).

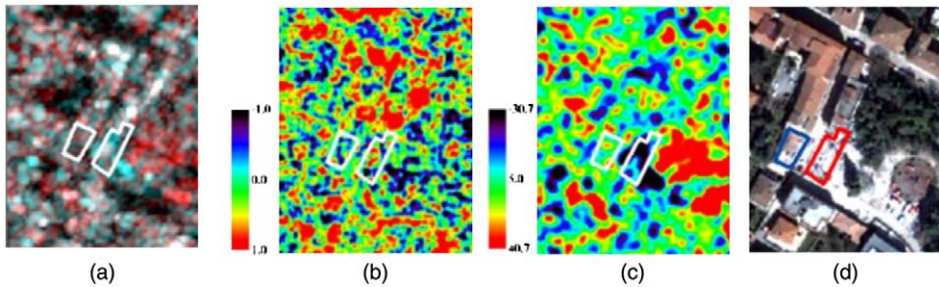


**Figure 8.** Close-up of area C in Figure 4. (a) RGB color composite of calibrated SAR images (R: the post-event, G, B: the pre-event), (b) the correlation coefficient, (c) the backscattering difference, and (d) the post-event QuickBird image (2009.4.8).

positive and negative backscatter values, respectively. Due to the effects of nearby damaged (G4) and collapsed (G5) buildings, the correlation value is seen to increase. The post-event QuickBird image is also shown in Figure 8d for comparison.

It is often the case that once a building is collapsed (or severely damaged) due to an earthquake, a radar sensor will receive less backscatter from the building, compared to its intact state. However, contradictory observation also can happen. As shown schematically in Figure 6, when a collapsed building is surrounded by intact buildings, there is an increase of travel path of radar signals from the collapsed building than from smooth/flat roof surfaces, which might cause an increase of the SAR backscattering intensity. Three different cases are shown for easy understanding. In Figure 9b, we can see that collapsed buildings had shown positively higher backscatter. From a plan layout of the city, it can be observed that buildings with similar heights were standing very closely to each other, thus producing weak backscattering from the continuous roofs. Once these buildings are damaged, their roofs are no longer at the same level as before, leading to diffuse backscattering. This

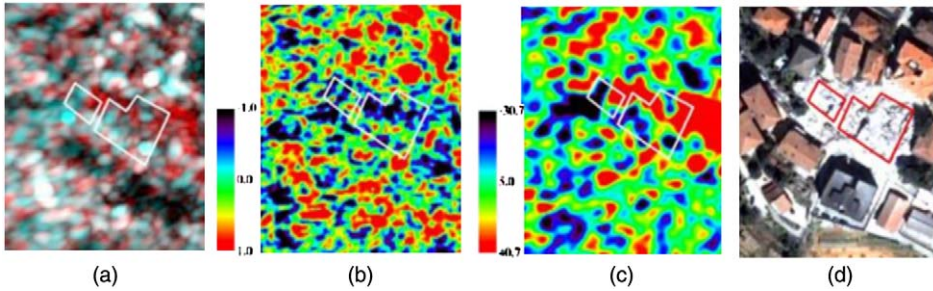


**Figure 9.** Close-up of area D in Figure 4. (a) RGB color composite of calibrated SAR images (R: the post event, G, B: the pre-event), (b) the correlation coefficient, (c) the backscattering difference, and (d) the post-event QuickBird image (2009.4.8).

may explain the increased backscatter from the area of damaged buildings, adjacent to intact buildings. Similar observations were found in Balz and Liao (2010) and Matsuoka and Yamazaki (2010).

The threshold value for low correlation was selected as 0.18, which gave the highest overall accuracy from the cumulative distribution plots of the two classes of damage (Figure 10). A building was judged as Grade 5 if its correlation value was less than 0.18, otherwise judged as less damage (Grades 1 to 4). When a threshold correlation value of 0.18 was used to discriminate the damage status of buildings, we could correctly find out the 6 collapsed buildings (Grade 5) out of 8, corresponding to the producer accuracy of 75%. Similarly out of 110 less damaged buildings (Grades 1–4), we could correctly find 100 corresponding with the 90.9% producer accuracy. The error of omission for G5 buildings was 25%, while the error of commission was 62.5%. The high commission error is partially

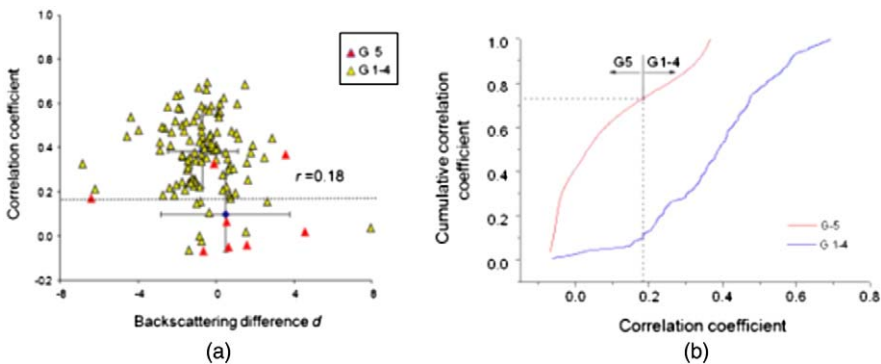


**Figure 10.** (a) Plot of the correlation  $r$  and the backscattering difference  $d$  for each building footprint of G1–4 (yellow symbol) and G5 (red symbol), where the mean and error bar with one standard deviation are also shown. (b) Cumulative frequency of the correlation coefficient for Grade 5 (red line) and Grades 1–4 (blue line) buildings.

due to the small number of G5 buildings compared with G1–4 buildings. Some less-damaged buildings were also observed as the collapsed buildings, which might be due to the effects of vegetation since X-band is highly affected by vegetation. Similarly, because the radar is of a side-looking nature, it inherently contains geometric errors, such as layover, radar foreshortening, and shadowing (Campbell 2002). In an urban area, layover is common, as the response from the top of a building comes earlier to the satellite than that from its base. Regarding the user accuracy for the Grade 5 buildings, it was 37.5 %, while for less damage (Grades 1–4), it was 98.0%. Overall accuracy from our damage detection method was 89.8%, and the Kappa value was 0.45. The Kappa coefficient of 0.45 refers that the observed classification is 45% better than one resulting from the chance. Therefore, we can say that there is a moderate level of agreement between the analysis and truth data. The result of analysis is given in the error matrix tabulated in Table 1 and shown in Figure 11.

We also applied our threshold of correlation to discriminate the collapsed and less-damaged buildings (G1–4) in two new blocks within the study area for accuracy assessment. The truth data for this was obtained from the visual observation of the pre- and post-event QuickBird images as well as from [Tertulliani et al. \(2010\)](#), as shown in Figure 12. In block F, there were 8 buildings: one G5, and rest seven G1–4. We could correctly classify both the collapsed (G5) and less damaged buildings (G1–4). In block G, there were 33 buildings: 1 G5 and 32 G1–4 buildings. We could correctly find the collapsed building (G5); however, regarding the G1–4 buildings, we could find 31 correctly, but misdetection of one as collapsed (G5) was found. This misdetection might be due to the presence of tall trees in front of this building.

If we compare the results with previous studies regarding the accuracy, [Matsuoka and Yamazaki \(2004\)](#) had reached 78% of overall accuracy when they used the damage detection for the 1995 Kobe earthquake using 30 m-resolution ERS/SAR images. However, the method they used was in a block level while our method extracted the pixels satisfying the damage condition within a building footprint for damage detection. Similarly, [Dell'Acqua et al. \(2010\)](#) conducted building damage assessment using only a post-event COSMO/SkyMed image for the L'Aquila earthquake based on texture in a block level utilizing the damage

**Table 1.** Error matrix for damage detection

		Truth data				
		Collapsed (Grade 5)	Less damage (Grades 1–4)	Total	User accuracy (%)	
Results from damage detection from TerraSAR-X	Collapsed (Grade 5)	6	10	16	37.5	
	Less damage (Grades 1–4)	2	100	102	98.0	
	Total	8	110	118	–	
	Producer accuracy (%)	75	90.9		–	
	Overall accuracy (%)				89.8	–
	Kappa coefficient					0.45

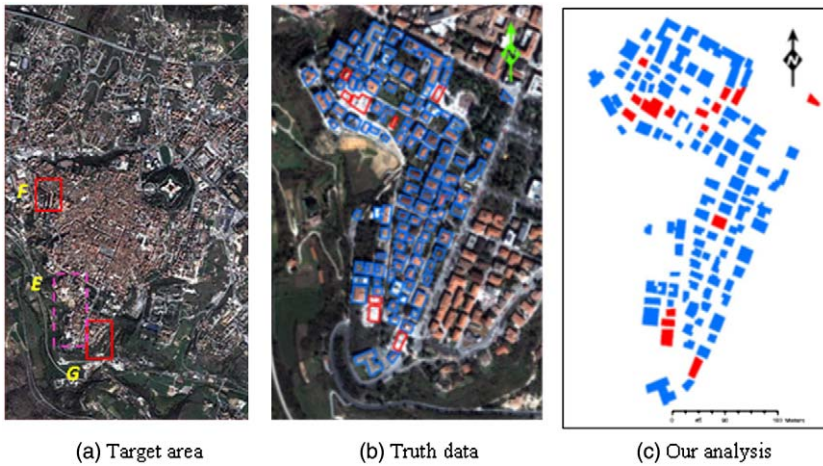


**Figure 11.** Close-up of area E (marked by dotted pink polygon in Figure 4 and also shown in (a)) showing the comparison of our analysis data (c) with truth data (b). Red polygons in (b) show the collapsed buildings (Grade 5) while blue polygons represent less damaged (Grades 1–4) buildings. Red filled polygons in (c) are the possible collapsed buildings using our threshold value. Six out of eight G5 buildings were correctly identified by our analysis.

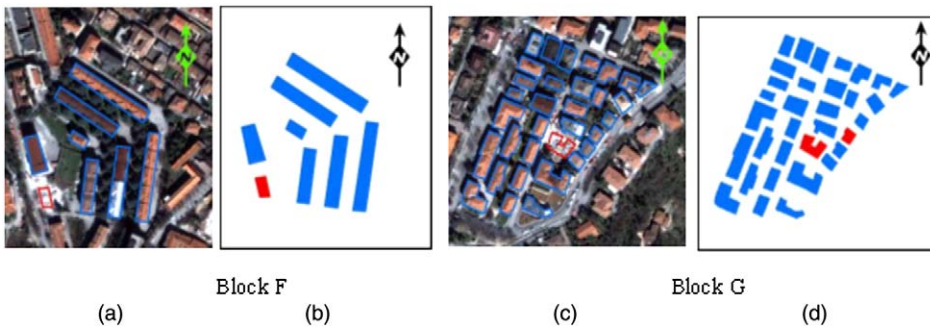


**Figure 12.** Application of threshold value of  $r$  in two different blocks F and G as shown in Figure 11a. Comparison of our analysis results in (b) and (d) with visual damage detection results in (a) and (c) is shown. Red polygons in (a) and (c) show the collapsed buildings (Grade 5) while blue polygons represent less damaged (Grades 1–4) buildings. Red filled polygons in (b) and (d) are the possible collapsed buildings using our threshold value.

area ratio (DAR). Brunner et al. (2010) used pre-event optical and post-event SAR data to perform damage detection after the May 2008 Sichuan, China, earthquake. They used 30 buildings as a dataset and reached overall accuracy of 90%. Our overall accuracy is also similar to it. These comparisons show the effectiveness of our proposed approach. To replicate this method in other areas, however, more case studies for similar urban settings are necessary.

## CONCLUSION

The advent of high-resolution SAR images has opened up new possibilities in different avenues, including damage detection in an emergency phase. One of the new possibilities of high-resolution TerraSAR-X is that it can be employed in minute change detection in urban areas. In this study, we have carried out the building damage detection at an individual building level using high-resolution TerraSAR-X data in the 2009 L'Aquila earthquake. The study area was chosen in the city center of L'Aquila. L'Aquila is an old city with dense urban agglomeration in the city core; however, in the periphery of city core, a sparsely built-up area exists. Because of the complex interaction of radar backscatter, damage detection at an individual level could not be done in the highly dense city core. However, we were able to perform damage detection at an individual level in the sparsely built-up area.

For this purpose, the correlation coefficient was calculated from the SAR intensity images taken before and after the earthquake. These values were then obtained for all building footprints under consideration and the values were averaged within the footprint. The obtained results were compared with the truth data and with the pre-and post-event Quick-Bird images. We could correctly classify collapsed buildings and less-damaged buildings in a rather sparsely built-up area of L'Aquila with producer accuracy of 75% and overall accuracy of 89.8% with a Kappa coefficient of 0.45. Although urban areas are rather difficult targets for damage extraction, the high-resolution SAR showed its capability in emergency operations. For the replication of this method in other areas, more case studies for similar urban settings are necessary.

## ACKNOWLEDGMENTS

The TerraSAR-X images used in this study were made available from SAR Application Research Committee, organized by PASCO Corporation, Tokyo, Japan. The ground truth data used were provided by Italian Civil Protection Agency.

## REFERENCES

- Balz, T., and Liao, M., 2010. Building damage detection using post-seismic high-resolution SAR satellite data, *International Journal of Remote Sensing* **31**, 3369–3391.
- Brunner, D., Lemoine, G., and Bruzzone, L., 2010. Earthquake damage assessment of buildings using VHR optical and SAR imagery, *IEEE Transactions on Geoscience and Remote Sensing* **48**, 2423–2430.
- Breit, H., Fritz, T., Balss, U., Lachaise, M., Niedermeier, A., and Vonavka, M., 2010. TerraSAR-X SAR processing and product, *IEEE Transaction on Geoscience and Remote Sensing* **48**, 727–740.
- Brown, L. G., 1992. A survey of image registration techniques, *ACM Computing Surveys* **24**, 325–376.
- Casarotti, C., Pavese, A., and Paleso, S., 2010. Seismic response of the San Salvatore hospital of Coppito (L'Aquila) during the earthquake of April 6th 2009, *Progettazione Sismica* **1**, 159–172.
- Cambell, J. B., 2002. *Introduction to Remote Sensing*, 3rd edition, Taylor & Francis, New York, 621 pp.

- Celebi, M., Bazzurro, P., Chiaraluce, L., Clemente, P., Decanini, L., Adriano, D., Ellsworth, W., Gorini, A., Kalkan, E., Marcucci, S., Milan, G., Mollaioli, F., Olivieri, M., Paolucci, R., Rinaldis, D., Rovelli, A., Sabetta, F., and Stephens, C., 2010. Recorded motions of the 6 April 2009 Mw 6.3 L'Aquila, Italy, earthquake and implications for building structural damage: overview, *Earthquake Spectra* **26**, 651–684.
- Congalton, R. G., 1991. A review of assessing the accuracy of classifications of remotely sensed data, *Remote Sensing of Environment* **37**, 35–46.
- Cosenza, E., Manfredi, G., and Verderame, G. M., 2010. Reinforced concrete buildings, *Progettazione Sismica* **1**, 131–147.
- Dell'Acqua, F., Gamba, P., Lisini, G., and Polli, D., 2010. Satellite remote sensing as a tool for emergencies from natural disasters; a case study on the earthquake of April 6th 2009 of L'Aquila, *Progettazione Sismica* **1**, 85–94.
- Fidani, C., 2010. The earthquake lights (EQL) of the 6 April 2009 L'Aquila earthquake, in central Italy, *Natural Hazards and Earth System Sciences* **10**, 967–978.
- Gamba, P., and Dell'Acqua, F., 2007. Rapid damage detection in the Bam area using multi-temporal SAR and exploiting ancillary data, *IEEE Transactions on Geoscience and Remote Sensing* **45** (6), 1582–1589.
- German Aerospace Center (DLR), 2009. TerraSAR-X Ground Segment Basic Specification Document, TX-GS-DD-3302. V1.6.
- Huyck, C. K., Mansouri, B., Eguchi, R. T., Houshmand, B., Castner, L. L., and Shinozuka, M., 2002. Earthquake damage detection algorithm using optical and ERS-SAR satellite data—application to the August 17, 1999 Turkey earthquake, *Proceeding of the 7th National US Conference on Earthquake Engineering*, Boston, MA.
- Infoterra, 2008. Radiometric calibration of TerraSAR-X data, TXX-ITD-TN-0049, available at <http://www.infoterra.de> (last accessed on 10 February 2010).
- Lee, J. S., 1980. Digital image enhancement and noise filtering by use of local statistics, *IEEE Transaction, Pattern Analysis and Machine Intelligence, Photographic Surveying and Remote Sensing PAMI-2*, 165–168.
- Liu, W., Yamazaki, F., Gokom, H., and Koshimura, S., 2012. Extraction of flooded areas and damaged buildings due to the tsunami of Japan 2011 Tohoku earthquake, *Proceedings of the IEEE 2012 International Geoscience and Remote Sensing Symposium, IEEE*, CD-ROM.
- Lillesand, T. M., Kiefer, R. W., and Chipman, J. W., 2004. *Remote Sensing and Image Interpretation*, John Wiley & Sons, New York, 804 pp.
- Matsuoka, M., and Yamazaki, F., 2004. Use of satellite SAR intensity imagery for detecting building areas damaged due to earthquakes, *Earthquake Spectra* **20**, 975–994.
- Matsuoka, M., and Yamazaki, F., 2010. Comparative analysis for detecting areas with building damage from several destructive earthquakes using satellite synthetic aperture radar images, *Journal of Applied Remote Sensing, SPIE*, **4**, 1–16.
- Rathje, E., and Adams, B., 2008. The role of remote sensing in earthquake science and engineering: opportunities and challenges, *Earthquake Spectra* **24**, 471–492.
- Saito, K., Spence, R., Going, C., and Markus, M., 2004. Using high-resolution satellite images for post-earthquake building damage assessment: a study following the 26 January 2001 Gujarat earthquake, *Earthquake Spectra* **20**, 145–169.
- Stramondo, S., Bignami, C., Chini, M., Pierdicca, N., and Tertulliani, A., 2006. Satellite radar and optical remote sensing for earthquake damage detection: results for different case studies, *International Journal of Remote Sensing* **27**, 4433–4447.

- Stucchi, M., Meletti, C., Ravida, A., D'Amio, V., and Capera, A., 2010. Historical earthquakes and seismic hazard of the L'Aquila area, *Progettazione Sismica* **1**, 23–34.
- Thao, N. V., Lan, D. T., Huong, D. T., and Ve, N. D., 2010. Assessing damage of flood by using ALOS data in Thua Thien-Hue province, *The 4th Joint PI symposium of ALOS Data nodes for ALOS Science Program*, Tokyo, Japan, 125.
- Tertulliani, A., Arcoraci, L., Berardi, M., Bernardini, F., Camassi, R., Castellano, C., Del Mese, S., Ercolani, E., Graziani, L., Leschiutta, I., Rossi, A., and Vecchi, M., 2011. An application of EMS98 in a medium-sized city: the case of L'Aquila (Central Italy) after the 6 April 2009 Mw 6.3 earthquake, *Bulletin of Earthquake Engineering* **9**, 67–80.
- United Nations Office for Disaster Reduction (ISDR), 2010. *Terminology*, available at <http://www.unisdr.org/we/inform/terminology> (last accessed on 10 February 2010).
- United States Geological Survey (USGS), 2010. *Shakemap us2009fcaf*, available at <http://earthquake.usgs.gov/earthquakes/shakemap/global/shake/2009fcaf/> (last accessed on 10 February 2010).
- Yamazaki, F., Yano, Y., and Matsuoka, M., 2005. Visual damage interpretation of buildings in Bam city using QuickBird images following the 2003 Bam, Iran earthquake, *Earthquake Spectra* **21**, S329–S336.
- Yonezawa, C., and Takeuchi, S., 2001. Decorrelation of SAR data by urban damages caused by the 1995 Hyogoken-Nanbu earthquake, *International Journal of Remote Sensing* **22**, 1585–1600.

(Received 2 June 2011; accepted 20 August 2012)